Approaches for Continuous-Time Dynamic Modeling of the Asymmetric Dual-Active Half-Bridge Converter

Shiladri Chakraborty, *Student Member, IEEE*, Manas Palmal and Souvik Chattopadhyay, *Member, IEEE*
Department of Electrical Engineering
Indian Institute of Technology Kharagpur
Kharagpur - 721302, India
Email: shiladri@ee.iitkgp.ernet.in

***Abstract*—This paper describes two continuous-time approaches for modeling the dual-active half-bridge converter, operated with 3D control i.e control involving variation of the duty-ratios of the two half-bridge legs along with the phase-shift. The first full-order model, based on generalized averaging, results in a model capable of approximately predicting both the fast inductor current dynamics and the slow capacitor voltage dynamics of the converter and is applicable to any generic case of 3D control. The second approach, based on simple averaging, results in a reduced-order model capable of predicting the slow voltage dynamics with greater accuracy. The demerit of this approach is the difficulty in extending it to other modes of operation, which limits its usability for 3D control. This problem is circumvented by focussing the analysis on the optimum high-frequency operating modes, which yield the best converter efficiency. Relevant transfer functions using both approaches are plotted and verified by comparing them with results obtained from PLECS simulation studies.**

I. Introduction

The half-bridge version of the popular dual-active-bridge (DAB) topology [1] is widely used in high efficiency, isolated, bi-directional dc-dc power conversion applications in the low power regime (typically below 750 W). Fig. 1 shows the schematic of such a dual active half-bridge (DAHB) converter used in uni-directional power flow applications, with one of the dc ports connected to an R-C load. Compared to its full-bridge counterpart, the DAHB converter offers the additional benefits of low device count, reduced size and operation with zero steady-state dc offset of magnetizing current.

Simplest operation of a DAB or DAHB converter involves driving both primary and secondary half-bridges with a 50 % duty-ratio and varying the phase overlap between the resulting square waves to regulate power flow. This scheme, referred to as simple-phase-shift control (SPC) in this paper, results in high circulating current and loss of zero-voltage-switching (ZVS) operation when the effective voltage-conversion ratio (v/nV_{g1}) is non-unity [1]. Significant improvement in converter performance is possible by utilizing the duty-ratios of the primary or secondary side bridges or both as additional control handles [2], [3]. Key representative steady-state waveforms for globally optimal operation corresponding to the most generic control strategy, referred to as 3D control in this paper, are depicted in Fig. 2. In all these cases, a satisfactory dynamic model of the converter is necessary to enable proper design of a closed-loop feedback controller.

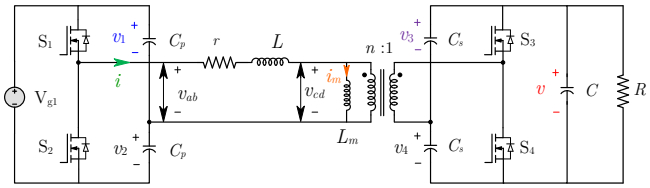

Fig. 1: The Dual Active Half-bridge (DAHB) converter with R-C load. The five independent states required to completely model the converter are emphasized with the colored symbols.

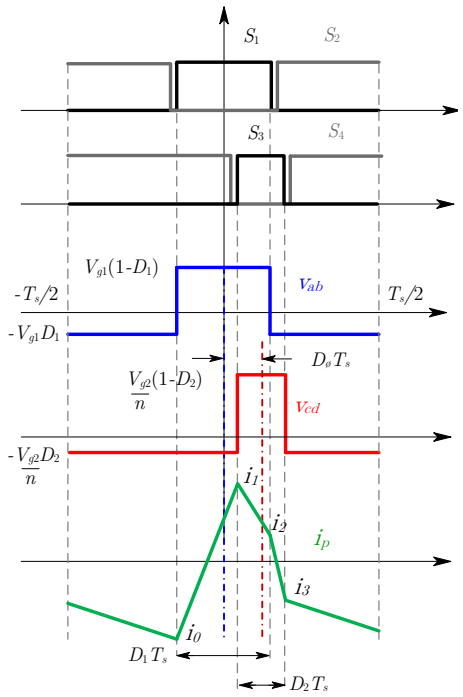

Fig. 2: Key steady-state waveforms for operation with 3D control. D_1, D_2 and D_ϕ are the control variables. $S_1 - S_4$ denote switching functions of the devices.

Classical approaches for modeling power electronic converters can be broadly classified as - a) discrete-time methods and b) continuous-time methods. Discrete-time models, as in [4], [5] are more suitable for the present-day digital controllers and are more accurate at higher frequencies. But they provide less design insights on account of their complex formulations [6]. Continuous-time models based on the state-space averaging technique require the small-ripple approximation to be satisfied. Hence they can be applied, as in [7], [8] to model only the slowly varying states having low switching ripple viz. the capacitor voltages. In order to model the sub-cycle variations of the inductor current (i), a generalized averaging approach, as discussed in [10], [11] needs to be adopted.

Modeling techniques of DAHB converters reported in literature [7], [9] are focussed on predicting low-frequency excursions of slowly varying state variables with the converter operated under SPC or 2D asymmetric operation. This paper considers the problem of deriving continuous-time, small-signal dynamic models of asymmetrically driven DAHB converters. Two modeling methodologies are considered. The first approach follows the generalized averaging method to propose a full-order model, capable of predicting transformer current dynamics. The converter is assumed to be operated with 3D control and hence the obtained model is an unified one, applicable in any general case, like [12]. The second approach, based on simple averaging, yields a reduced-order model which can model the capacitor average voltage dynamics more accurately. In the following section, both approaches are discussed in detail and their relative merits and demerits are pointed out.

II. Modeling of the converter

A. Switched model

The exact time-domain behaviour of the converter is governed by the following five differential equations, corresponding to the independent states depicted in Fig. 1. These equations constitute the starting point of both modeling approaches discussed in the following sections.

$$\begin{aligned} L\frac{di}{dt} &= v_{ab} - v_{cd} - ir \\ &= v_{g1}(S_1 - 1) + v_1 - nv(S_3 - 1) - nv_3 - ir. \end{aligned} \quad (1)$$

$$L_m\frac{di_m}{dt} = v_{cd} = nv(S_3 - 1) + nv_3. \quad (2)$$

$$i = -2C_p\frac{dv_1}{dt}. \quad (3)$$

$$\begin{aligned} n(i - i_m) &= C_s\frac{dv_3}{dt} - C_s\frac{dv_4}{dt}. \\ &= 2C_s\frac{dv_3}{dt} - C_s\frac{dv}{dt}. \end{aligned} \quad (4)$$

$$i_{S3} = n(i - i_m)S_3 = C_s\frac{dv_3}{dt} + C\frac{dv}{dt} + \frac{v}{R}. \quad (5)$$

In the above equations, S_1 and S_3 represent the switching functions of the top switches of the primary and secondary half-bridge legs respectively, while i_{S3} denotes the current in the switch S_3 flowing from source to drain.

B. Generalized averaging-based model

The basic idea behind generalized averaging is to approximate a state variable by the sum of its average component and higher order harmonic components. For the simplest analysis, the fundamental harmonic approximation (FHA) is commonly applied [10] and only the switching frequency component is considered amongst all the harmonic components. Since in a typical design, the magnetizing current and capacitor voltages have negligible switching-frequency ripple, they are well approximated by their average values (over the switching time period T_s) only. However, for the inductor current (i), in addition to its average value i_0, the fundamental (switching frequency) component must also be considered to account for its sub-switching cycle variations. Also, the switching functions S_1 and S_3 must themselves be approximated by the sum of their dc and fundamental components. This results in the following relations.

$$S_1 = \langle S_1\rangle_0 + \langle S_1\rangle_1 = d_1 + \frac{2}{\pi}\sin(d_1\pi)\cos\omega_s t. \quad (6)$$

$$S_3 = \langle S_3\rangle_0 + \langle S_3\rangle_1 = d_2 + \frac{2}{\pi}\sin(d_2\pi)\cos(\omega_s t - d_\phi 2\pi). \quad (7)$$

$$i = i_0 + i_{1m}\cos(\omega_s t - \theta). \quad (8)$$

$$v_1 = v_{10}; v_3 = v_{30}; v = v_0; i_m = i_{m0}, \quad (9)$$

where $\langle x\rangle_0$, $\langle x\rangle_1$ respectively denote the average (over switching period) and fundamental component of any variable "x". Substituting the above relations in (1) - (5) results in the following seven non-linear large signal equations.

$$L\frac{di_0}{dt} = v_{g1}(d_1 - 1) + v_{10} - nv_0(d_2 - 1) - nv_{30} - i_0 r. \quad (10a)$$

$$L\frac{di_{1m}}{dt} = \frac{2}{\pi}v_{g1}\sin(d_1\pi)\cos\theta - \frac{2}{\pi}nv_0\sin(d_2\pi)\cos\beta - i_{1m}r. \quad (10b)$$

$$L\frac{d\theta}{dt} = -\frac{2}{\pi i_{1m}}v_{g1}\sin(d_1\pi)\sin\theta + \omega_s - \frac{2}{\pi i_{1m}}nv_0\sin(d_2\pi)\sin\beta. \quad (10c)$$

$$L_m\frac{di_{m0}}{dt} = nv_0(d_2 - 1) + nv_{30}. \quad (11)$$

$$i_0 = -2C_p\frac{dv_{10}}{dt}. \quad (12)$$

$$\frac{dv_{30}}{dt} = \left(\frac{d_2C_s + C}{C_{eq}C_s}\right) n(i_0 - i_{m0}) - \frac{1}{RC_{eq}} v_0 + \frac{1}{\pi C_{eq}} n i_{1m} \sin(d_2\pi)\cos\beta. \quad (13)$$

$$\frac{dv_0}{dt} = \left(\frac{2d_2 - 1}{C_{eq}}\right) n(i_0 - i_{m0}) - \frac{2}{RC_{eq}} v_0 + \frac{2}{\pi C_{eq}} n i_{1m} \sin(d_2\pi)\cos\beta, \quad (14)$$

where $C_{eq} = (2C + C_s)$ and $\beta = (d_\phi 2\pi - \theta)$. It may be pointed out at this stage that in the full-bridge DAB converter, i_0 is not considered as an additional state because, as mentioned in [10], provided the initial value of i_0 is zero and circuit non-idealities (like unmatched device voltage drop, gate-drive delay etc. [13]) are absent, i_0 remains zero even in the dynamic state. In a DAHB converter, however, as (12) indicates, i_0 must be considered to be non-zero in the dynamic state in order to model the average voltage dynamics of the primary side half-bridge capacitors.

The large-signal equations (10) through (14) can be perturbed and linearized about a steady operating point to obtain the small-signal model of the system in the standard state-space form $\dot{\hat{x}} = A_{fos}\hat{x} + B_{fos}\hat{u}$, where $x = [\ v_{30}\ v_{10}\ v_0\ i_0\ i_{1m}\ \theta\ i_{m0}\ ]^T$ represents the state vector and $u = [\ d_\phi\ d_1\ d_2\ v_{g1}\ ]^T$ is the input vector. From these, a variety of control input or disturbance input to output transfer functions can be found. The small signal matrices A_{fos}, B_{fos} are presented in Appendix B.

C. Reduced-order model

Often the objective of the modeling exercise is to predict the dynamic behaviour of only the slowly varying capacitor voltages. In such a scenario, instead of the computationally complex seventh order model derived above, a relatively simpler fifth order model can be used which replaces the inductor current i only by its average value i_0. Capacitor voltages and magnetizing currents are approximated by their average values, as previously. Using these approximations, the basic switched model equations (1) - (5) can be written in the following fashion after simplification.

$$L\frac{di_0}{dt} = v_{g1}(d_1 - 1) + v_{10} - nv(d_2 - 1) - nv_{30} - i_0 r\ . \quad (15)$$

$$L_m\frac{di_{m0}}{dt} = nv_0(d_2 - 1) + nv_{30}\ . \quad (16)$$

$$\frac{dv_{10}}{dt} = -\frac{i_0}{2C_p}\ . \quad (17)$$

$$2C_s\frac{dv_{30}}{dt} - C_s\frac{dv_0}{dt} = n(i_0 - i_{m0})\ . \quad (18)$$

$$C\frac{dv_0}{dt} + C_s\frac{dv_{30}}{dt} + \frac{v_0}{R} = \langle i_{S3}\rangle_0 = n\langle (i - i_m)S_3\rangle_0\ . \quad (19)$$

where $L_{eq} = LL_m/(L + L_m)$ and $\langle i_{S3}\rangle_0$ denotes the average value of i_{S3}. The complete large-signal model can be obtained provided a closed-form expression relating $\langle i_{S3}\rangle_0$ with the state variables and inputs can be derived. This step presents considerable computational difficulty, since the expression for $\langle i_{S3}\rangle_0$ depends on the mode of circuit operation, determined by the relative values of d_1, d_2 and d_ϕ. As detailed in [3], as many as fifteen operating modes exist for generic 3D control. Hence deriving the large signal model involves the evidently cumbersome task of rewriting the expression for $\langle i_{S3}\rangle_0$ for each mode. This repetitive computational complexity somewhat limits the practical applicability of this modeling method. To circumvent this problem, circuit operation in only two high-frequency modes are considered in this paper, which are defined as follows

$$0 < d_2 < d_1 < 0.5,\ (d_1 - d_2)/2 < d_\phi < (d_1 + d_2)/2, \quad (20a)$$

$$0 < d_1 < d_2 < 0.5,\ (d_2 - d_1)/2 < d_\phi < (d_1 + d_2)/2. \quad (20b)$$

These two modes, denominated as modes 1b and 2b respectively in [3], are considered because, as discussed in [3], appropriate circuit operation in these modes can lead to globally minimum transformer rms current operation while also ensuring ZVS operation of all switches. The expression for $\langle i_{S3}\rangle_0$ in both of these modes is given by

$$\langle (i - i_m)S_3\rangle_0 = (i_0 - i_{m0})d_2 + \frac{v_{g1}}{k}\Big[\frac{{d_2}^2 - {d_1}^2}{8} + \frac{d_\phi}{2}(d_1 d_2^{'} - d_\phi) + \frac{d_1 d_2}{4}(d_1 - d_2)\Big] + \frac{v_{10} - nv_{30}}{k}. \quad (21)$$
$$\frac{d_2}{4}(d_1 - d_2 + 2d_\phi) - \frac{nv_0}{k}.\frac{d_2 d_2^{'}}{4}(d_2 - d_1 - 2d_\phi)\ .$$

where $k = Lf_s$ and $d_2^{'} = (1 - d_2)$. Equations (15) through (19) and (21) constitute the non-linear large signal equations of the reduced order (fifth-order) model, which may be perturbed and linearized as before to obtain the small-signal linear model. The corresponding small signal matrices A_{ros}, B_{ros} are provided in Appendix A. The state and input vectors are $x = [\ v_{30}\ v_{10}\ v_0\ i_0\ i_{m0}\ ]^T$ and $u = [\ d_\phi\ d_1\ d_2\ v_{g1}\ ]^T$ respectively. Since circuit operation with square-wave control (SPC) is a special case of operation in mode 1b/ 2b with $d_1 = d_2 = 0.5$, the small-signal matrices for SPC can be obtained by substituting $d_1 = d_2 = 0.5$ in the relevant expressions.

III. Results and discussions

Small-signal control to output transfer functions, obtained using both methods, have been generated using MATLAB for the parameter values specified in Tab. I. The selected operating point ($D_1 = 0.4$, $D_2 = 0.3$, $D_\phi = 0.2$) corresponds to operation in mode 1b and thus the developed fifth order model can be used. Further, a switched circuit model of the converter has been developed in the simulation platform PLECS and using the approach outlined in [10], points on relevant Bode

TABLE I: PARAMETER VALUES FOR THE SIMULATION MODEL

V_{g1}	f_s	r	L	L_m
200 V	50 KHz	100 mΩ	20 μH	250 μH

C_p	C_s	C	R	Turns-ratio (n)
10 μF	20 μF	500 μF	19.5 Ω	1:1

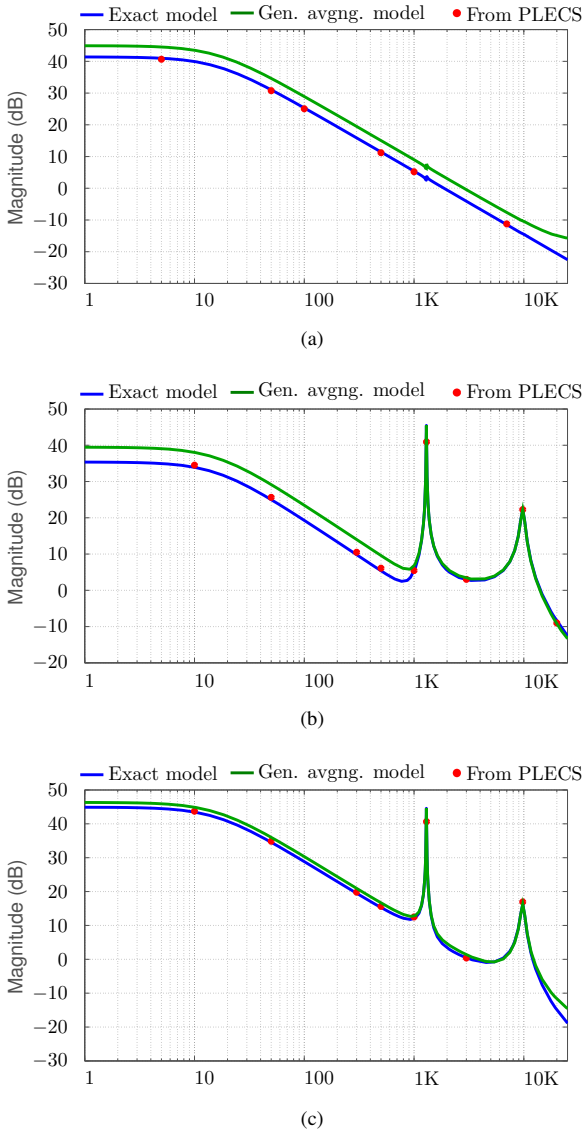

Fig. 3: Bode plots of small-signal *control to output voltage* transfer functions obtained from the FHA-based generalized averaging model (green) and the exact fifth-order model (blue) for D_1 = 0.4, D_2 = 0.3, D_ϕ = 0.2. (a) $\widehat{v}_0(s)/\widehat{d}_\phi(s)$, (b) $\widehat{v}_0(s)/\widehat{d}_1(s)$, (c) $\widehat{v}_0(s)/\widehat{d}_2(s)$. X axis is frequency in Hz. Small-signal gains computed at some discrete perturbation frequencies using PLECS are overlaid with the red circles.

plots have been generated to verify the results obtained from analysis. Some of these plots are presented in Fig. 3 - 5.

Fig. 3 shows the Bode plots of the control-to-output voltage transfer functions. It is observer that while the predictions of

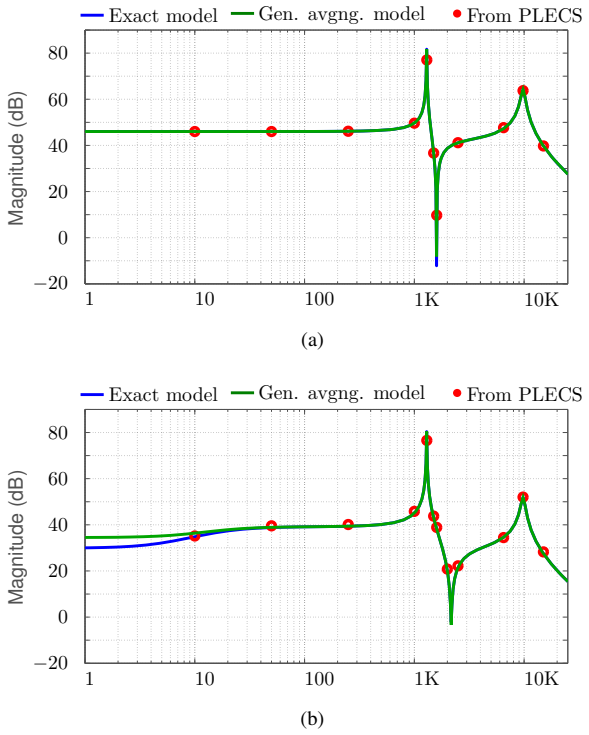

Fig. 4: Bode plots of *duty-ratio to half-bridge capacitor voltage* transfer functions obtained from the FHA-based generalized averaging model (green) and the exact fifth-order model (blue) for D_1 = 0.4, D_2 = 0.3, D_ϕ = 0.2. (a) $\widehat{v}_{10(s)}/\widehat{d}_1(s)$, (b) $\widehat{v}_{30}(s)/\widehat{d}_2(s)$. PLECS data points are shown in red, as before.

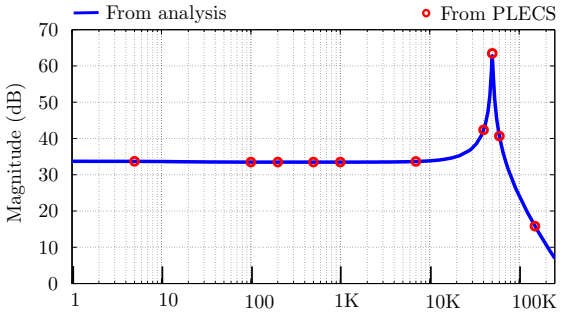

Fig. 5: Bode plot of *phase-shift to transformer current fundamental amplitude* transfer function $(\widehat{i}_1(s)/\widehat{d}_\phi(s))$ obtained from the generalized averaging model (blue) for D_1 = 0.4, D_2 = 0.3, D_ϕ = 0.2. PLECS data points are shown in red, as before.

the fifth-order model match exactly with values obtained from PLECS across the frequency range, there is a steady dc error associated with the generalized averaging-based model in the low frequency range. This inaccuracy can be attributed to the fundamental harmonic approximation, which neglects power -flow due to the higher harmonic components.

Bode plots of the duty-ratio of the two legs to the corresponding upper half-bridge capacitor voltages are depicted in Fig. 4. The predictions of both the fifth-order and the seventh-order models are found to be quite accurate in this case. Using empirical verifications, the L and C components contributing to produce the two resonant peaks, observable in the plots of

Fig. 3 and 4, can be deduced. The first of these peaks arises due to resonance between L_m and $C_{eq1} = 2(C_p + C_s/n^2)$, while the second one is due to resonance between L and $C_{eq2} = 2(C_pC_s/n^2)/(C_p + C_s/n^2)$, with the height of the peaks being proportional to the transformer's winding resistance r. Finally, a plot of the phase-shift to inductor current inductor current fundamental amplitude small-signal transfer function, obtained using the generalized averaging method, is shown in Fig. 5.

Comparison of some time-domain simulation results of the generalized averaging-based model with the exact switched model are presented in Fig. 6-8. Fig. 6 shows the steady-state transformer current waveform, which is reasonably well approximated by the generalised average model. A more accurate representation of the high-frequency current waveform may be obtained by inclusion of additional harmonics, at the cost of increased complexity of the model. Fig. 7, 8 illustrate the dynamic response of the capacitor voltages when a step change in V_{g1} is applied. It is observed that the average model is able to predict the low-frequency dynamics of the voltages, with some steady-state error, arising due to the fundamental harmonic approximation, as explained previously.

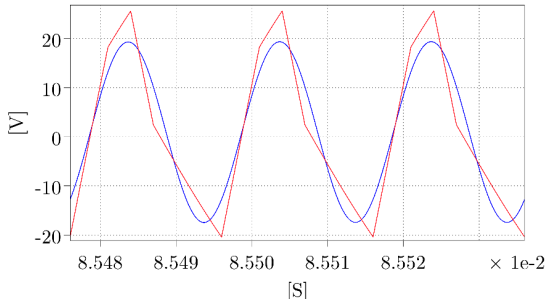

Fig. 6: Steady-state transformer current waveform. (red - exact switched model, blue - generalized average model.)

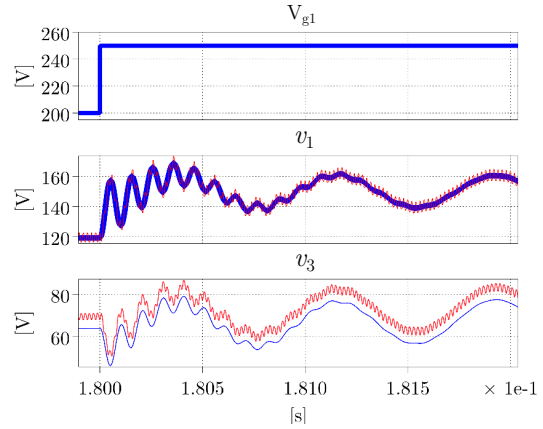

Fig. 7: Dynamic response of primary and secondary side top capacitor voltages. (red - exact switched model, blue - generalized average model.)

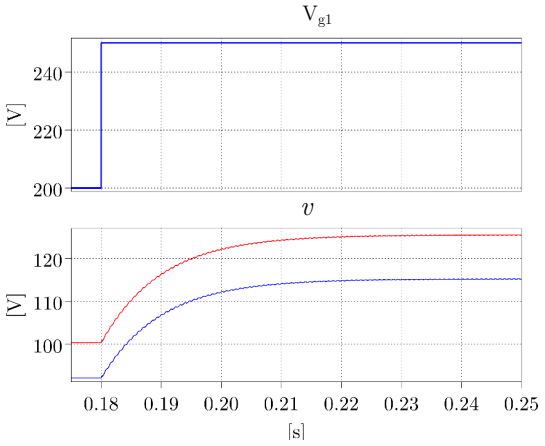

Fig. 8: Dynamic response of output voltage. (red - exact switched model, blue - generalized average model.)

IV. Conclusion

Two approaches for continuous-time modeling of a DAHB converter have been discussed in this paper. The first approach, based on the generalized averaging method uses the fundamental harmonic approximation to represent the piecewise linear inductor current waveform by a switching frequency component. This approach yields a seventh-order model which can be readily applied to any case of asymmetric 3D control and can approximately predict the high-frequency dynamics of the inductor current. The demerit of this approach is its reduced accuracy at low frequencies, especially for the control to output voltage transfer functions. The second approach, based on direct averaging of the output current waveform, yields a fifth-order model, which agrees exactly with PLECS simulation results throughout the frequency range. The fundamental limitation of this approach is the difficulty to extend it to any case of 3D control, because of the need to re-write the expression for average output current for each mode of operation. This problem is circumvented in this work by analysing only a specific operating mode, which is known to result in the least transformer rms current and also ensure ZVS of the switches.

References

[1] M. H. Kheraluwala, R.W. Gascoigne, D.M. Divan and E. D. Baumann, "Performance characterization of a high-power dual active bridge dc-dc converter," *IEEE Trans. Ind. Appl.*, 28(6), pp. 1294-1301, Nov./Dec. 1992.

[2] S. Chakraborty and S. Chattopadhyay, "Minimum-RMS-Current Operation of Asymmetric Dual Active Half-Bridge Converters With and Without ZVS," *IEEE Trans. Power Electron.*, 32(7), pp. 5132-5145, Jul. 2017.

[3] S. Chakraborty, S. Tripathy and S. Chattopadhyay, "Minimum RMS Current Operation of the Dual-Active Half-Bridge Converter using Three Degree of Freedom Control," *Energy Conversion Congress and Exposition (ECCE), 2016 IEEE*, Sept. 2016.

[4] D. Costinett, R. Zane and D. Maksimovic, "Discrete-time small-signal modeling of a 1 MHz efficiency-optimized dual active bridge converter with varying load," *Workshop on Control and Modeling for Power Electronics (COMPEL), 2012 IEEE*, pp. 1-7, June 2012.

[5] F. Krismer and J. W. Kolar, "Accurate Small-Signal Model for the Digital Control of an Automotive Bidirectional Dual Active Bridge," *IEEE Trans. Power Electron.*, 24(12), pp. 2756-2768, Dec. 2009.

[6] R. B. Ridley, "A New, Continuous-Time Model For Current-Mode Control," *IEEE Trans. Power Electron.*, 6(2), pp. 271-280, April. 1991.

[7] M. Wang, Y. Du, S. Lukic and A. Q. Huang, "Small-signal analysis and modeling of the Dual Active Half Bridge converter," *Applied Power Electronics Conference and Exposition (APEC), 2012 IEEE*, pp. 1833-1837, Feb. 2012.

[8] H. Bai, C. Mi, C. Wang and S. Gargies, "The Dynamic Model and Hybrid Phase-Shift Control of a Dual-Active-Bridge Converter," *Industrial Electronics Conference (IECON), 2008 IEEE* , pp. 2840-2845, Nov. 2008.

[9] H. Li and F. Z. Peng, "Modeling of a New ZVS Bi-directional DC-DC Converter," *IEEE Trans. Aerosp. Electron. Syst.*, pp. 272-283, Jan. 2004.

[10] H. Qin and J. W. Kimball, "Generalized Average Modeling of Dual Active Bridge DC-DC Converter," *IEEE Trans. Power Electron.*, 24(12), pp. 2078-2084, Apr. 2012.

[11] S. S. Shah and S. Bhattacharya, "Large & small signal modeling of dual active bridge converter using improved first harmonic approximation," *Applied Power Electronics Conference and Exposition (APEC), 2017 IEEE*, pp. 1175-1182, Mar. 2017.

[12] D. Seltzer, L. Corradini, D. Bloomquist, R. Zane and D. Maksimovic, "Small signal phasor modeling of dual active bridge series resonant DC/DC converters with multi-angle phase shift modulation," *Energy Conversion Congress and Exposition (ECCE), 2011 IEEE*, pp. 2757-2764, Sept. 2011.

[13] G. Ortiz, L. Fassler, J. W. Kolar and O. Apeldoorn, "Flux Balancing of Isolation Transformers and Application of the Magnetic Ear for Closed-Loop Volt-Second Compensation," *IEEE Trans. Power Electron.*, vol. 29, no. 8, pp. 4078–4090, Aug. 2014.

[14] Y. Yin, R. Zane, J. Glaser and R. W. Erickson "Small-signal analysis of frequency-controlled electronic ballasts," *IEEE Trans. Circuits and Systems I*, 50(8), pp. 1103-1110, Aug. 2003.

APPENDIX A
SMALL-SIGNAL MATRICES OF THE FIFTH-ORDER MODEL FOR OPERATION IN MODE 1B/2B

$\dot{\hat{x}} = A_{ros}\hat{x} + B_{ros}\hat{u}$, where $x = [\ v_{30}\ v_{10}\ v_0\ i_0\ i_{m0}\ ]^T$ and $u = [\ d_\phi\ d_1\ d_2\ v_{g1}\ ]^T$.

$$A_{ros} = \begin{bmatrix} -F_1 & \frac{F_1}{n} & -\Big(F_2 + \frac{1}{RC_{eq}}\Big) & F_3 & -F_3 \\ 0 & 0 & 0 & -\frac{1}{2C_p} & 0 \\ -2F_1 & \frac{2F_1}{n} & -2\Big(F_2 + \frac{1}{RC_{eq}}\Big) & F_4 & -F_4 \\ -\frac{n}{L} & \frac{1}{L} & \frac{n(1-D_2)}{L} & -\frac{r}{L} & 0 \\ \frac{n}{L_m} & 0 & -\frac{n(1-D_2)}{L_m} & 0 & 0 \end{bmatrix}$$

$C_{eq} = 2C + C_s$, $D_2{}' = 1 - D_2$, $F_1 = \dfrac{n^2 D_2(D_1 - D_2 + 2D_\phi)}{4Lf_sC_{eq}}$,

$F_2 = \dfrac{n^2 D_2 D_2{}'(D_2 - D_1 - 2D_\phi)}{4Lf_sC_{eq}}$, $F_3 = \dfrac{n}{2C_s} + \dfrac{2nD_2 - n}{2C_{eq}}$,

$F_4 = \dfrac{2nD_2 - n}{C_{eq}}$.

$$B_{ros} = \begin{bmatrix} nG_1 & nG_2 & nG_3 & nG_4 \\ 0 & 0 & 0 & 0 \\ 2nG_1 & 2nG_2 & 2nG_3 & 2nG_4 \\ 0 & \frac{V_{g1}}{L} & -\frac{nV_0}{L} & -\frac{1-D_1}{L} \\ 0 & 0 & \frac{nV_0}{L_m} & 0 \end{bmatrix}$$

$$G_1 = \frac{V_{g1}(D_1{}'D_2 + D_1D_2{}' - 2D_\phi)}{2Lf_sC_{eq}},$$

$$G_2 = \frac{V_{g1}(D_1{}'D_2 + 2D_1D_2 + 2D_2{}'D_\phi - D_1 - {D_2}^2)}{4Lf_sC_{eq}},$$

$$G_3 = \frac{(V_{10} - V_{30})(D_1 + 2D_\phi - 2D_2)}{4Lf_sC_{eq}} - \frac{V_0[2D_2 - 3{D_2}^2 - (1 - 2D_2)(D_1 + 2D_\phi)]}{4Lf_sC_{eq}} + \frac{V_{g1}(D_2 + {D_1}^2 - 2D_1D_2 - 2D_1D_\phi)}{4Lf_sC_{eq}},$$

$$G_4 = \frac{({D_2}^2 - {D_1}^2)/8}{Lf_sC_{eq}} + \frac{D_\phi/2(D_1D_2{}' - D_\phi)}{Lf_sC_{eq}} + \frac{D_1D_2/4(D_1 - D_2)}{Lf_sC_{eq}}.$$

APPENDIX B
SMALL-SIGNAL MATRICES OF THE FHA-BASED SEVENTH ORDER MODEL

$\dot{\hat{x}} = A_{fos}\hat{x} + B_{fos}\hat{u}$, where $x = [\ v_{30}\ v_{10}\ v_0\ i_0\ i_{1m}\ \theta\ i_{m0}\ ]^T$ and $u = [\ d_\phi\ d_1\ d_2\ v_{g1}\ ]^T$.

$$A_{fos} = \begin{bmatrix} 0 & 0 & -\frac{1}{RC_{eq}} & n.\left(\frac{C+D_2C_s}{C_sC_{eq}}\right) & n.\frac{\gamma}{\pi C_{eq}} & n.\frac{I_1\zeta}{\pi C_{eq}} & -n.\left(\frac{C+D_2C_s}{C_sC_{eq}}\right) \\ 0 & 0 & 0 & -\frac{1}{2C_P} & 0 & 0 & 0 \\ 0 & 0 & -\frac{2}{RC_{eq}} & n.\left(\frac{2D_2-1}{C_{eq}}\right) & n.\frac{2\gamma}{\pi C_{eq}} & n.\frac{2I_1\zeta}{\pi C_{eq}} & -n.\left(\frac{2D_2-1}{C_{eq}}\right) \\ -\frac{n}{L} & \frac{1}{L} & n\left(\frac{1-D_2}{L}\right) & -\frac{r}{L} & 0 & 0 & 0 \\ 0 & 0 & -\frac{2n\gamma}{\pi L} & 0 & -\frac{r}{L} & -\frac{2}{\pi L}\left(V_{g1}\delta + nV_0\zeta\right) & 0 \\ 0 & 0 & -\frac{2n\zeta}{\pi LI_1} & 0 & \frac{2}{\pi LI_1^2}\left(V_{g1}\delta + nV_0\zeta\right) & \frac{2}{\pi LI_1}\left(-V_{g1}\rho + nV_0\gamma\right) & 0 \\ \frac{n}{L_m} & 0 & n\left(\frac{D_2-1}{L_m}\right) & 0 & 0 & 0 & 0 \end{bmatrix}$$

$$B_{fos} = \begin{bmatrix} -\frac{2nI_1\zeta}{C_{eq}} & 0 & \frac{nI_1\gamma\cot(D_2\pi)}{C_{eq}} & 0 \\ 0 & 0 & 0 & 0 \\ -\frac{4nI_1\zeta}{C_{eq}} & 0 & \frac{2nI_1\gamma\cot(D_2\pi)}{C_{eq}} & 0 \\ 0 & \frac{V_{g1}}{L} & -\frac{nV_0}{L} & \left(\frac{D_1-1}{L}\right) \\ \frac{4nV_0\zeta}{L} & \frac{2}{L}V_{g1}\rho\cot(D_1\pi) & -\frac{2nV_0\gamma\cot(D_2\pi)}{L} & \frac{2\rho}{\pi L} \\ -\frac{4nV_0\gamma}{I_1L} & -\frac{2}{I_1L}V_{g1}\delta\cot(D_1\pi) & -\frac{2}{I_1L}nV_0\zeta\cot(D_2\pi) & -\frac{2\delta}{\pi LI_1} \\ 0 & 0 & \frac{nV_0}{L_m} & 0 \end{bmatrix}$$

where $\gamma = \sin(D_2\pi)\cos\beta_0$, $\zeta = \sin(D_2\pi)\sin\beta_0$, $\delta = \sin(D_1\pi)\sin\theta_0$, $\rho = \sin(D_1\pi)\cos\theta_0$, $\beta_0 = (2\pi D_\phi - \theta_0)$.
$D_1, D_2, D_\phi, \beta_0$ and θ_0 represent quiescent values of respective variables.